



Spring melt pond fraction in the Canadian Arctic Archipelago predicted from RADARSAT-2

Stephen E.L. Howell¹, Randall K. Scharien², Jack Landy³ and Mike Brady¹

5 ¹Climate Research Division, Environment and Climate Change Canada, Toronto, M3H 5T4, Canada

²Department of Geography, University of Victoria, Victoria, V8W 2Y2, Canada

³School of Geographical Sciences, University of Bristol, Bristol, BS8 1QU, United Kingdom

Correspondence to: Stephen E.L. Howell (Stephen.Howell@Canada.ca)

10 **Abstract.** Melt ponds form on the surface of Arctic sea ice during spring, influencing how much solar radiation is absorbed into the sea ice-ocean system, which in turn impacts the ablation of sea ice during the melt season. Accordingly, melt pond fraction (f_p) has been shown to be a useful predictor of sea ice area during the summer months. Sea ice dynamic and thermodynamic processes operating within the narrow channels and inlets of the Canadian Arctic Archipelago (CAA) during the summer months are difficult for model simulations to accurately resolve. Additional information on f_p variability in advance of the melt season within the CAA could help constrain model simulations and/or provide useful information in advance of the shipping season. Here, we use RADARSAT-2 imagery to predict and analyze peak spring f_p and evaluate its utility to provide predictive information with respect to sea ice area during the melt season within the CAA from 2009-2018. The temporal variability of RADARSAT-2 f_p over the 10-year record was found to be strongly linked to the variability of mean April multi-year ice area and the spatial distribution of RADARSAT-2 f_p was found to be in excellent agreement with the sea ice stage of development prior to the melt season. RADARSAT-2 f_p values were in good agreement with the peak f_p observed from *in situ* observations but were found to be ~0.05 larger compared to peak MODIS f_p observations. Statistically significant detrended correlations between RADARSAT-2 f_p and summer sea ice area were found for several regions within the CAA. Our results show that RADARSAT-2 f_p can be used to provide predictive information about summer sea ice area for a key shipping region of the Northwest Passage.

25

1 Introduction

Arctic sea ice extent during the summer months has declined considerably over the satellite record (Serreze et al., 2007; Stroeve et al., 2012; Peng and Meier, 2017). Surface melt ponds, which form on sea ice during the spring, play an important role in the decay of sea ice and seasonal reduction in ice extent because they influence how much solar radiation is absorbed into the sea ice-ocean system (Eicken et al., 2004). Specifically, the accumulation of meltwater on the surface of the sea ice lowers the albedo from ~0.8 to between 0.2-0.4 and enhances melt (Perovich et al., 2002). The topographical constraints over multi-year ice (MYI) imposed by hummocks typically result in MYI exhibiting a lower melt pond fraction



(f_p) compared to seasonal first-year ice (FYI) (Grenfell and Perovich, 2004; Polashenski et al., 2012; Landy et al., 2015). With Arctic sea ice transitioning from a MYI to FYI dominated icescape (Maslanik et al., 2011), the lower f_p of MYI will
35 gradually be replaced with the higher f_p of FYI, facilitating even more sea ice energy absorption and further enhancing sea ice melt (Perovich and Polashenski, 2012).

Predicting the state of Arctic sea ice several months in advance is challenging and recently, the sea ice prediction community has focused efforts on the development and utilization of dynamical forecast models (e.g. Chevallier et al., 2013; Sigmund et al., 2013; Guemas et al., 2016). Despite these recent efforts, rapidly changing Arctic sea ice conditions will
40 continue to necessitate improved sea ice forecasting capabilities (Eicken, 2013). Accordingly, prognostic f_p schemes have been integrated in climate models and have shown to exert a strong influence on summer sea ice area and extent (Flocco et al., 2010; Flocco et al., 2012). Schröder et al. (2014) found a strong correlation between model-simulated May f_p and the observed September sea ice extent. Observed f_p has also demonstrated significant predictive skill for September ice extent from late-July onwards (Liu et al., 2015). However, while f_p estimates for the entire Arctic can be provided by model
45 simulations, more representative and higher spatial resolution observational estimates at regional and pan-Arctic scales are much more difficult to obtain.

Optical remote sensing is the most widely utilized approach to estimate large-scale f_p from space (e.g. Markus et al., 2003; Tschudi et al., 2008; Rösel et al., 2012; Istomina et al., 2014; Webster et al., 2015; Lee et al., 2020) but cloud cover remains a significant problem. Techniques for retrieving f_p using advanced quad-polarization and compact-polarization mode
50 synthetic aperture radar (SAR) imagery, at C- and X-band frequencies, have also been developed (Scharien et al., 2014; Fors et al., 2017; Li et al., 2017) but they are limited in systematic spatial application because the required polarization modes are not always available from wide-swath imagery. However, using the winter backscatter from widely available Sentinel-1 SAR imagery, Scharien et al. (2017) recently demonstrated a technique for predicting spring f_p over the entire Canadian Arctic Archipelago (CAA) 3-4 months in advance of melt pond formation. These f_p predictions have potential utility in
55 seasonal summer sea ice area and extent forecasts as early as April.

The CAA is a collection of islands located in Northern Canada (Figure 1) whose waterways are sea ice covered between fall and spring. It is an active region for marine shipping and has recently experienced an increase in summer shipping activity (Pizzolato et al., 2014). Model simulations have been utilized to understand the current and predicted future variability of sea ice conditions in the CAA (e.g. Dumas et al., 2006; Sou and Flato, 2009, Howell et al., 2016; Laliberté et al., 2016; Hu et al., 2018; Laliberté et al., 2018) but it still remains challenging because complex sea ice dynamic and thermodynamic processes are often not accurately resolved in its narrow channels and inlets. In addition, the response of the CAA to climatic change is perhaps counter-intuitive as longer melt seasons are resulting in increased MYI import from the Arctic Ocean during the summer months (Howell and Brady, 2019). Since f_p is linked to summer sea ice melt processes (e.g. Eicken et al., 2004; Skillingstad and Polashenski, 2018) additional information on f_p variability within the CAA could
65 improve our understanding of regional summer melt processes, help constrain model simulations and facilitate safer shipping activity in upcoming years.



In this study, we extend the work of Scharien et al. (2017) and investigate predicted f_p variability within the CAA over the longer-term record available from RADARSAT-2. Specifically, (i) we estimate the predicted seasonal peak f_p in the CAA using RADARSAT-2, (ii) evaluate the spatiotemporal variability of f_p in the CAA from 2009-2018 (iii) compare RADARSAT-2 f_p values to Sentinel-1 f_p values from Scharien et al. (2017), *in situ* f_p observations from Landy et al. (2014) and Moderate Resolution Image Spectroradiometer (MODIS) f_p values from Rösel et al. (2012) and (iv) investigate the utility of RADARSAT-2 f_p to provide predictive information about sea ice area in the CAA during the summer melt season.

2 Methodology

2.1 Data

The primary dataset used in this analysis was 5.405 GHz (wavelength, $\lambda = 5.5$ cm; C-band) SAR imagery in ScanSAR wide mode at HH polarization from RADARSAT-2 acquired over the CAA (Figure 1) in April from 2009-2018 (Table 1). RADARSAT-2 ScanSAR wide mode imagery has a spatial resolution of 100 m with an incidence angle range of 20.0° to 49.3°.

In situ observations of melt pond fraction on landfast FYI were obtained in two consecutive years from sites in the CAA using a terrestrial Light Detection and Ranging (LiDAR) system (Landy et al., 2014) (Figure 1, green star). In 2011, the site was located in Allen Bay on FYI with relatively rough surface topography, whereas in 2012, the site was located in Resolute Passage on FYI with relatively smooth topography. At each site, a time-series of f_p observations were collected within the same 100 x 200 m area of the ice over a 2 to 3 week period following melt onset, covering three of the four stages of melt pond evolution detailed in Eicken et al. (2004). The LiDAR system produces dense measurements over snow or sea ice with specular reflection over melt ponds allowing melt pond fractions to be retrieved with an accuracy better than 5% (Landy et al., 2014). These observations allow us to evaluate how well predicted f_p from RADARSAT-2 resolve the peak f_p of seasonally-evolving sea ice coverage.

We also made use of 8-day composite satellite observations of f_p obtained from the MODIS Arctic melt pond cover fractions dataset for the period of 2009-2011 (Rösel et al., 2012) and weekly sea ice area and stage of development observations obtained from the Canadian Ice Service Digital Archive (CISDA) regional ice charts for the period of 2009-2018 (Tivy et al., 2011).

2.2 Estimating f_p from RADARSAT-2

RADARSAT-2 f_p was determined using a modified approach to that described by Scharien et al. (2017). Their approach determines the second stage of the seasonal melt pond evolution cycle when f_p is at its peak (Eicken et al., 2003; Polashenski et al., 2012) using Sentinel-1 Extra Wide (EW) swath imagery obtained during April in within the CAA. April corresponds to late winter sea ice conditions in the CAA, when sea ice growth has reached its maximum and spring warming has yet to begin. Their approach was developed by relating the winter period HH gamma nought (γ^p) backscatter in decibel (dB) from Sentinel-1 to peak f_p observations in 1.7 m spatial resolution GeoEye-1 imagery, from spatially coincident image



segments that represented homogeneous FYI and MYI regions. The result was that γ° can be converted to f_p using the following equation:

$$f_p = -0.221 - 0.041(\gamma^\circ) \quad (1)$$

In equation (1), γ° was found to explain 73% of the variability in f_p (Scharien et al., 2017).

105 In this study, all the available HH polarization RADARSAT-2 imagery over the CAA in April from 2009-2018 (Table 1) were first calibrated to γ° which minimizes the influence of incidence angle more so than with sigma nought (σ°) (Small, 2011). RADARSAT-2 images were then speckle filtered using a 5x5 Lee Filter and spatially registered to a common map projection. Finally, γ° was converted to f_p by applying Equation (1) to each RADARSAT-2 image. For each year, the corresponding RADARSAT-2 f_p images in April were mosaicked together to cover the entire spatial domain of the CAA.
110 Constructing a mosaic over a large region such as the CAA presents certain challenges with SAR imagery, particularly incidence angle variability. Even with the use of γ° , Scharien et al. (2017) found that because of varying incidence angles associated with different ScanSAR images that f_p striping can still occur within the CAA in the mosaicked image. Our approach here was to average out incidence angle variability by taking advantage of large amount of overlapping RADARSAT-2 imagery within the CAA (i.e. 90 to 159 images; Table 1) together with the fact that the majority of the sea
115 ice in the CAA is landfast (immobile) during April which results in a temporally stable f_p for all April images. To produce a RADARSAT-2 f_p mosaic within the CAA for each year, we calculated the mean f_p for each overlapping pixel using all of each year's RADARSAT-2 April images that effectively helped to reduce f_p striping across the CAA.

The root-mean square error (RMSE) of f_p based on equation (1) is 0.085 (Scharien et al., 2017). While calculating the mean f_p of the overlapping image pixels helps reduce striping across the CAA, it also adds additional uncertainty and its
120 effectiveness depends on the number of overlaps. In order to quantify the additional uncertainty ($RMSE_{R2}$), we used the mean and maximum standard deviation of RADARSAT-2 f_p of all pixels within the CAA calculated from 2009-2018 (f_{std}) together with a range of pixel overlaps (n) in the following equation:

$$RMSE_{R2} = [(f_{std}/n^{0.5})^2 + 0.085^2]^{0.5} \quad (2)$$

Since RADARSAT-2 imagery is acquired operationally, overlapping images vary interannually but pixel overlaps across the
125 CAA were typically between 6-12. Figure 2 illustrates the $RMSE_{R2}$ values for a range of pixel overlaps using the 2009-2018 mean f_{std} value of 0.08 and the 2009-2018 maximum f_{std} value of 0.2. For the maximum f_{std} with pixel overlaps between 6-12 the $RMSE_{R2}$ ranges from 0.10-0.12.

3 Results and Discussion

130 3.1 RADARSAT-2 f_p spatial and temporal variability from 2009-2018

The spatial distribution of mosaicked RADARSAT-2 f_p and pre-melt season (i.e. April) and sea ice stage of develop conditions in the CAA for the 2009-2018 time period are shown in Figures 3 and 4, respectively. Lower f_p values are located primarily in the northern regions of the CAA (Queen Elizabeth Islands), Viscount-Melville Sound and the M'Clintock



Channel where the majority of the CAA's MYI is typically found. The shallow bays and narrow channels located throughout
135 the CAA exhibit high f_p values and these regions are typically associated with smooth FYI whereas rougher ice regions (i.e.
Gulf of Boothia) are associated with lower f_p values. We should expect a lower f_p over MYI regions compared to FYI regions
(Grenfell and Perovich, 2004; Perovich and Polashenski, 2012) and indeed the overall spatial distribution of RADARSAT-2
 f_p is in excellent agreement with the spatial distribution of sea ice stage of development prior to the melt season for all years.

Figure 5a shows the time series of RADARSAT-2 f_p variability together with mean April MYI area in the CAA
140 from 2009-2018. Over the 10-year record, the mean RADARSAT-2 f_p was 0.47 and ranged from a low of 0.43 in 2009 to a
high of 0.52 in 2013. The temporal variability in RADARSAT-2 f_p is reflected in the variability of April MYI area within the
CAA over the 10-year record with a statistically significant detrended correlation (R) of $R=-0.89$. The RADARSAT-2 f_p
linkage with April MYI area is particularly evident from 2011 and 2012 which were very light sea ice years within the CAA
whereby a considerable amount of the CAA's MYI area was lost during the summer melt season (Howell et al., 2013) and
145 this resulted in 2012 and 2013 (i.e. the years following extreme melt) being the two highest RADARSAT-2 f_p years from
2009-2018 (Figure 3d-e). MYI area within in the CAA then increased following these light ice years and RADARSAT f_p
began to respond accordingly. In fact, there has always been a period of MYI recovery following light ice years with either
MYI grown *in situ* and/or advected from Arctic Ocean into the CAA and gradually migrating to the CAA's southern regions
(Howell et al., 2013). Figure 5b illustrates the standard deviation of RADARSAT-2 f_p from 2009-2018 and spatially reflects
150 the process of MYI flowing southward through the CAA as RADARSAT-2 f_p was more variable in the MYI regions of the
CAA compared to regions where FYI dominates the regional icescape.

What is interesting from the time series in Figure 5a is that from 2014-2018, with the exception of 2016, there was
more MYI area in April compared to 2009 yet the RADARSAT-2 f_p was not as low as in 2009. In addition, 2017 and 2018
also exhibited a larger spatial coverage of MYI compared to 2009 (Figure 4a, 4i-j). We suggest that higher RADARSAT-2 f_p
155 in recent years is a result of Arctic Ocean MYI entering the CAA being younger and thinner than in 2009 (Howell and
Brady, 2019) with smoother surface topography, thereby having a higher summer melt pond coverage (Landy et al., 2015).
This seems to be particularly evident particularly in the Viscount-Melville Sound and M'Clintock Channels regions when
comparing 2009 (Figure 3a) with 2017 (Figure 3i) and 2018 (Figure 3j). Indeed, several studies have reported considerable
decreases in the age and thickness of Arctic Ocean MYI north of the CAA in recent years (e.g. Kwok, 2018; Petty et al.,
160 2020; Tschudi et al., 2020)

3.2 Comparison of RADARSAT-2 f_p with and Sentinel-1, *in situ* and MODIS

Frequency distributions of RADARSAT-2 f_p and Sentinel-1 f_p from Scharien et al. (2017) in the CAA for 2016 and
2017 are shown in Figure 6. Sentinel-1 appears to estimate more regions of lower f_p compared to RADARSAT-2 which are
165 typically associated with MYI. Whereas, RADARSAT-2 estimates more regions of higher f_p which are typically associated
with FYI. Overall, there is good agreement between both sensors, as expected since both are C-band SAR with nearly
identical frequencies.



The *in situ* evolution of f_p over FYI within the CAA acquired by Landy et al. (2014) and illustrated in Figure 7 allows us to place the RADARSAT-2 f_p estimates within the melt pond stages of development classification system. Unfortunately, no MODIS f_p observations are located in close proximity to the *in situ* observations. The evolution of melt ponds on the surface of the sea ice has been classified into four distinct and consecutive stages. A brief description is provided here, and the reader is referred to Eicken et al. (2004) and Polashenski et al. (2012) for a more comprehensive description. In stage I, meltwater from snow melt fills topographic depressions on the surface of the sea ice until the ponds reach their maximum areal extent. In stage II, melt pond coverage decreases due to horizontal water transport into macroscopic flaws and drainage through the ice. In stage III, the melt ponds typically drain through to the ocean and further changes in melt pond coverage depend on changes in surface topography and freeboard. Finally, in stage IV, melt ponds that survived the melt season refreeze and snow begins to accumulate on their surface. For 2011, RADARSAT-2 f_p corresponds to the end of stage I and beginning of stage II thus providing a very good representation of the seasonal peak of the f_p , when the melt pond control on heat uptake and ice decay, through the ice-albedo feedback, is greatest. For 2012, RADARSAT-2 f_p also corresponds to the end of stage I and beginning of stage II but is ~ 0.1 lower than *in situ* f_p values. This is likely due to the very high maximum f_p of 0.78 in 2012 as Scharien et al. (2017) found that equation (1) sometimes underestimates very high f_p due to the low γ° signal associated with very smooth FYI.

The seasonal time series of the 8-day composite MODIS f_p , the maximum seasonal MODIS f_p and the predicted RADARSAT-2 f_p for 2009-2011 is shown in Figure 8. MODIS f_p observations within the CAA indicate initial pond formation occurred in May for all years with peak f_p being reached in mid-July for 2009 and in early June for 2010 and 2011. Compared to the RADARSAT-2 f_p values, the peak MODIS f_p is ~ 0.09 smaller. We suggest this is likely because the predicted RADARSAT-2 f_p corresponds to the stage of the seasonal melt pond evolution cycle when f_p is at its peak for each pixel within the CAA. The MODIS f_p observations are determined weekly using 8-day composite image products that would include some melt pond formation and drainage processes prior-to, and after, the seasonal peak. Also, MODIS f_p observations give the time series of f_p therefore even the highest seasonal estimated MODIS f_p is reduced because while some regions of the CAA are at their seasonal peak but others are behind or ahead. Therefore, we also calculated the maximum f_p from MODIS regardless of timing during the melt season, for each pixel, also in Figure 7. These values more closely compare with the RADARSAT-2 f_p but are still ~ 0.05 smaller on average.

195 3.3 Influence of RADARSAT-2 f_p on summer sea ice conditions

In order to investigate if RADARSAT-2 f_p values can be used to provide predictive information for summer sea ice area within the CAA, we separated the CAA into numerous predefined subregions and then determined the detrended correlations between RADARSAT-2 f_p and weekly sea ice area from the CISDA regional ice charts in each region over the period of 2009-2018. We tested each week from the start of June to the end of September. The strongest correlation, together with the corresponding week of occurrence are shown in Figures 9a and 9b, respectively. All the strongest correlations are negative, indicating – as expected – that years with higher predicted f_p values are associated with lower sea ice area at a later



point in the summer. Higher f_p lower the area-averaged albedo of the ice surface leading to accelerated melt and lower sea ice concentrations (e.g. Perovich and Polashenski, 2012). There is considerable spatial variability in the strongest correlation across the CAA with relatively low correlations in the majority of the northern CAA and very low correlations in the eastern regions of the CAA. The regions of Kellet-Crozier ($R=-0.92$), Viscount-Melville Sound ($R=-0.73$), M'Clintock Channel ($R=-0.77$) and Norwegian Bay ($R=-0.78$) all exhibit statistically significant correlations above the 95% confidence level. In terms of timing for the statistically significant regions, RADARSAT-2 f_p correlated the strongest to weekly sea ice area in August for all regions except Norwegian Bay (Figure 9b). Compared to previous studies, the primary difference between using f_p values to predict summer sea ice conditions seems to be the timing of when the correlation is the strongest. Using simulated f_p values, Schröder et al. (2014) found the strongest correlation to September sea ice occurred for the May f_p . Liu et al. (2015) used observed MODIS f_p values and reported the strongest correlation to September sea ice in late July. Our findings suggest that methods such as these may be able to predict August sea ice area from f_p simulations or observations with higher confidence than September ice area, at least in the CAA.

Why is the relationship stronger in some regions of the CAA and weaker in others? RADARSAT-2 f_p values are determined from imagery acquired in April when ice conditions in the CAA are landfast (immobile) and do not evolve in concert with sea ice dynamics operating within the CAA. As a result, RADARSAT-2 f_p values will not be spatially representative of the region's ice conditions when region-specific dynamic breakup processes dominate over thermodynamics (i.e. *in situ* melt). In other words, the origin of the some of the ice in these regions during the summer melt season will be not always be the same as in April (i.e. pre-melt) when the initial RADARSAT-2 f_p value was determined. The time series of weekly detrended RADARSAT-2 f_p and weekly sea ice area for selected regions within the CAA is shown in Figure 10 and provides evidence for this regional dichotomy. In the Viscount-Melville Sound and M'Clintock regions the correlations gradually get stronger, reaching a peak in August. These regions are known to be immobile and stagnant (e.g. Melling, 2002) with the majority of breakup taking place in September which is when the relationship begins to degrade. The Kellet-Crozier is another stagnant region which supports that in the absence of considerable ice dynamics the relationship between RADARSAT-2 f_p and sea ice area is strong throughout the melt season. The time series in Penny Strait illustrates how the correlation gradually increase but when the region's dynamic break-up begins in July, ice is advected southward which degrades the correlation. This was also the case for other many regions in the northern CAA (not shown) as the flushing of sea ice southward from the northern CAA is a regular occurrence during the melt season (Melling, 2002; Howell et al., 2006). The low correlations in the south eastern regions of the CAA are also likely a function of ice dynamics as these regions of the CAA are known to be considerably influenced by currents and wind (Prinsenbergh and Hamilton, 2005) and sea ice speed in Lancaster Sound and Barrow Strait can reach 10 km day^{-1} (Agnew et al., 2008).

The strong and statistically significant correlation in the Viscount-Melville Sound region is encouraging as it is a key shipping region in the northern route of the Northwest Passage. To that end, we used linear regression to predict mean August sea ice area within Viscount-Melville Sound with the detrended RADARSAT-2 f_p values as a predictor. Figure 11 illustrates the results as compared to observations (detrended) from the CISDA ice charts for 2009-2018. There is reasonable



agreement between the predicted and observed sea ice area in the region with an RMSE of $18 \times 10^3 \text{ km}^2$ and an $R^2=0.44$. The largest discrepancies occurred for 2013 and 2014 with the RADARSAT-2 f_p model prediction resulting in too little sea ice area. Overall, within the Viscount-Melville Sound region of CAA exists period for which a significant statistical relationship exists between RADARSAT-2 f_p and the summer ice area before dynamic ice motion begins to corrode the relationship.

240

4 Conclusions

In this study we predicted and analyzed spring f_p using RADARSAT-2 within the CAA from 2009-2018. The spatial variability in RADARSAT-2 f_p was found to be excellent agreement with the spatial distribution of sea ice stage of development prior to the melt season as high (low) f_p values were associated with FYI (MYI) types. The temporal variability of RADARSAT-2 f_p over the 10-year record was significantly correlated to April MYI area, highlighting the importance of MYI within the CAA.

RADARSAT-2 f_p was found to be in good agreement with the f_p maximum extent observed *in situ* for 2011 but were slightly lower than 2012 when peak f_p was very large (> 0.7). Compared to peak MODIS f_p values, RADARSAT-2 f_p values were larger by ~ 0.05 . Based on our *in situ* comparison, RADARSAT-2 f_p maybe more representative of peak f_p within the CAA compared to the MODIS 8-day product that may capture a more time-averaged f_p . We also found excellent agreement between RADARSAT-2 and Sentinel-1 which suggests that combining both Sentinel-1 and the recently launched RADARSAT Constellation Mission (RCM) could facilitate pan-Arctic f_p estimates. The RCM will also facilitate continued investigation of additional metrics that when combined with γ° could further improve predicted f_p .

The results presented in this study also indicate that RADARSAT-2 f_p can provide predictive information about summer sea ice area in certain regions of the CAA. Specifically, the strong and statistically significant de-trended correlation in the Viscount-Melville Sound region demonstrates that RADARSAT-2 f_p estimates are useful for providing predictive information about summer sea ice area in the northern route of the Northwest Passage. This information could find utility in constraining regional model simulations (e.g. Lemieux et al., 2016). Alternatively, it could be advantageous to exploit the high spatial resolution of SAR and investigate if local-scale f_p estimates could enhanced knowledge of summer ice conditions in northern communities (e.g. Cooley et al., 2020). Ultimately, imagery from RCM will ensure our time series of RADARSAT-2 f_p estimates in the CAA will continue, gradually building statistics facilitating the development of more robust statistical relationships in upcoming years.

Data Availability

RADARSAT-2 imagery is available online for a fee from the Earth Observation Data Management System (<https://www.eodms-sgdot.nrcan-rncan.gc.ca>). RADARSAT-2 derived melt pond fraction is available through the lead author SELH (stephen.howell@canada.ca). MODIS Arctic melt pond cover fractions dataset available from the Integrated Climate Data Center (ICDC, <https://icdc.cen.uni-hamburg.de/>). The CISDA is available online from the Canadian Ice Service (CIS; [8](https://www.canada.ca/en/environment-climate-change/services/ice-forecasts-observations/latest-</p></div><div data-bbox=)



270 [conditions/archive-overview.html](#)). In situ melt pond data is available through contributing author JL
(jack.landy@bristol.ac.uk)

Author contributions

SELH wrote the manuscript with input from all authors. SELH and MB performed the analysis.

275

Competing interests

The authors declare that they have no conflict of interest.

Acknowledgements

280 Funding for RKS provided by Polar Knowledge Canada Science and Technology Program Grant NST-1718-0024 and
Marine Environmental Observation Prediction and Response Network (MEOPAR) project 1-02-02-012.5. JL is supported by
the European Space Agency Living Planet Fellowship “Arctic-SummIT” under Grant ESA/4000125582/18/I-NS and the
Natural Environment Research Council Grants “PRE-MELT” NE/T000546/1 and “Diatom-ARCTIC” NE/R012849/1.

References

- 285 Agnew, T., Lambe, A., and Long, D.: Estimating sea ice area flux across the Canadian Arctic Archipelago using enhanced
AMSR-E, *Journal of Geophysical Research*, 113, C10011, doi:10.1029/2007JC004582, 2008.
- Chevallier, M., Salas, D., Méliá, Y., Voldoire, A., Déqué, M., and Garric, G.: Seasonal forecasts of the pan-Arctic sea ice
extent using a GCM-based seasonal prediction system, *Journal of Climate*, 26, 6092–6104, doi:10.1175/JCLI-D-12-00612.1,
290 2013
- Cooley, S.W., Ryan, J.C., Smith, L.C. et al.: Coldest Canadian Arctic communities face greatest reductions in shorefast sea
ice. *Nature Climate Change*. <https://doi.org/10.1038/s41558-020-0757-5>, 2020.
- 295 Dumas, J. A., Flato, G.M., and Brown, R.D.: Future projections of landfast ice thickness and duration in the Canadian
Arctic, *Journal of Climate*, 19, 5175–5189, 2006.
- Eicken, H.: Ocean science: Arctic sea ice needs better forecasts, *Nature*, 497(7450), 431–433, doi:10.1038/497431a, 2013.
- 300 Eicken, H., Krouse, H.R., Kadko, D., Perovich, D.K.: Tracer studies of pathways and rates of meltwater transport through
Arctic summer sea ice, *Journal of Geophysical Research*, 107(C10), 8046, doi:10.1029/2000JC000583, 2002.
- Eicken, H., Grenfell, T.C., Perovich, D.K., Richter-Menge, J.A., and Frey, K.: Hydraulic controls of summer Arctic pack ice
albedo, *Journal of Geophysical Research*, 109, C08007, doi:10.1029/2003JC001989, 2004.
- 305 Flocco, D., Feltham, D.L., and Turner, A.K.: Incorporation of a physically based melt pond scheme into the sea ice
component of a climate model, *Journal of Geophysical Research*, 115, C08012, doi:10.1029/2009JC005568, 2010.



- 310 Flocco, D., Schröder, D., Feltham, D.L. and Hunke, E.C.: Impact of melt ponds on Arctic sea ice simulations from 1990 to 2007, *Journal of Geophysical Research*, 117, C09032, doi:10.1029/2012JC008195, 2012.
- Fors, A. S., Divine, D. V., Doulgeris, A. P., Renner, A. H. H., and Gerland, S.: Signature of Arctic first-year ice melt pond fraction in X-band SAR imagery, *The Cryosphere*, 11, 755–771, <https://doi.org/10.5194/tc-11-755-2017>, 2017.
- 315 Grenfell, T. C., and Perovich, D.K.: Seasonal and spatial evolution of albedo in a snow-ice-land-ocean environment, *Journal of Geophysical Research*, 109, C01001, doi:10.1029/2003JC001866, 2004.
- Guemas, V., Chevallier, M., Déqué, M., Bellprat, O., Doblus-Reyes, F.: Impact of sea ice initialization on sea ice and atmosphere prediction skill on seasonal timescales, *Geophysical Research Letters*, 43, 3889–3896, doi:10.1002/2015GL066626, 2016.
- 320 Howell, S.E.L., Tivy, A., Yackel, J.J., and Scharien, R.K.: Application of a SeaWinds/QuikSCAT sea ice melt algorithm for assessing melt dynamics in the Canadian Arctic Archipelago. *Journal of Geophysical Research-Oceans*, 111, C07025, doi:10.1029/2005JC003193, 2006.
- 325 Howell, S. E. L., Wohlleben, T., Komarov, A., Pizzolato, L., and Derksen, C.: Recent extreme light sea ice years in the Canadian Arctic Archipelago: 2011 and 2012 eclipse 1998 and 2007, *The Cryosphere*, 7, 1753–1768, <https://doi.org/10.5194/tc-7-1753-2013>, 2013.
- 330 Howell, S. E. L., Laliberté, F., Kwok, R., Derksen, C., and King, J.: Landfast ice thickness in the Canadian Arctic Archipelago from observations and models, *The Cryosphere*, 10, 1463–1475, <https://doi.org/10.5194/tc-10-1463-2016>, 2016.
- Howell, S. E. L., and Brady, M.: The dynamic response of sea ice to warming in the Canadian Arctic Archipelago. *Geophysical Research Letters*, 46, 13119– 13125. <https://doi.org/10.1029/2019GL085116>, 2019
- 335 Hu, X., Sun, J., Chan, T. O., and Myers, P. G.: Thermodynamic and dynamic ice thickness contributions in the Canadian Arctic Archipelago in NEMO-LIM2 numerical simulations, *The Cryosphere*, 12, 1233–1247, <https://doi.org/10.5194/tc-12-1233-2018>, 2018.
- 340 Istomina, L., Heygster, G., Huntemann, M., Schwarz, P., Birnbaum, G., Scharien, R., Polashenski, C., Perovich, D., Zege, E., Malinka, A., Prikhach, A., and Katsev, I.: Melt pond fraction and spectral sea ice albedo retrieval from MERIS data – Part 1: Validation against in situ, aerial, and ship cruise data, *The Cryosphere*, 9, 1551–1566, <https://doi.org/10.5194/tc-9-1551-2015>, 2015.
- 345 Kwok, R.: Arctic sea ice thickness, volume, and multiyear ice coverage: losses and coupled variability (1958–2018). *Environmental Research Letters*, 13, 105005, doi:10.1088/1748-9326/aae3ec, 2018.
- Laliberté, F., Howell, S.E.L. and Kushner, P.J.: Regional variability of a projected sea ice-free Arctic during the summer months, *Geophysical Research Letters*, 43, doi:10.1002/2015GL066855, 2016.
- 350 Laliberté, F., Howell, S. E. L., Lemieux, J.-F., Dupont, F., and Lei, J.: What historical landfast ice observations tell us about projected ice conditions in Arctic archipelagoes and marginal seas under anthropogenic forcing, *The Cryosphere*, 12, 3577–3588, <https://doi.org/10.5194/tc-12-3577-2018>, 2018.
- 355 Landy, J.C., Ehn, J.K., Shields, M. and Barber, D.G.: Surface and melt pond evolution on landfast first-year sea ice in the Canadian Arctic Archipelago, *Journal of Geophysical Research*, 119(5), 3054-3075, 2014.



- 360 Landy, J.C., Ehn, J.K., and Barber, D.G.: Albedo feedback enhanced by smoother Arctic sea ice, *Geophysical Research Letters*, 42(24), 710-714. doi:10.1002/2015GL066712, 2015.
- Lee, S., Stroeve, J.C., Tsamados, M. and Khand, A.L.: Machine learning approaches to retrieve pan-Arctic melt ponds from visible satellite imagery, *Remote Sensing of Environment*, <https://doi.org/10.1016/j.rse.2020.111919>, 2020.
- 365 Lemieux, J.-F., Beaudoin, C., Dupont, F., Roy, F., Smith, G.C., Shlyueva, A., Buehner, M., Caya, A., Chen, J., Carrieres, T., Pogson, L., DeRepentigny, P., Plante, A., Pestieau, P., Pellerin, P., Ritchie, H., Garric, G. and Ferry, N.: The Regional Ice Prediction System (RIPS): verification of forecast sea ice concentration. *Q.J.R. Meteorol. Soc.*, 142: 632-643. doi:10.1002/qj.2526, 2016.
- 370 Li, H., Perrie, W., Li, Q., and Hou, Y.: Estimation of melt pond fractions on first year sea ice using compact polarization SAR. *Journal of Geophysical Research*, 122, 8145–8166, <https://doi.org/10.1002/2017JC013248>, 2017.
- Liu, J., Song, M.H., Horton R.M., and Hu, Y.: Revisiting the potential of melt pond fraction as a predictor for the seasonal Arctic sea ice extent minimum, *Environmental Research Letters*, 10(5). <https://doi.org/10.1088/1748-9326/10/5/054017>, 2015.
- 375 Markus, T., Cavalieri, D.J., Tschudi, M.A., and Ivanoff, A.: Comparison of aerial video and Landsat 7 data over ponded sea ice, *Remote Sensing of Environment*, 86, 458–469, 2003.
- 380 Maslanik, J., Stroeve, J., Fowler, C., and Emery, W.: Distribution and trends in Arctic sea ice age through spring 2011, *Geophysical Research Letters*, 38, L13502, doi:10.1029/2011GL047735, 2011.
- Peng, G. and Meier, W.M.: Temporal and regional variability of Arctic sea-ice coverage from satellite data, *Annals of Glaciology*, 59(76pt2), 191-200. doi:10.1017/aog.2017.32, 2017.
- 385 Perovich, D. K., Grenfell, T.C., Light, B., and Hobbs, P.V.: Seasonal evolution of the albedo of multiyear Arctic sea ice, *Journal of Geophysical Research*, 107(C10), 8044, doi:10.1029/2000JC000438, 2002.
- 390 Petty, A. A., Kurtz, N.T., Kwok, R., Markus, T., and Neumann, T. A.: Winter Arctic sea ice thickness from ICESat-2 freeboards. *Journal of Geophysical Research: Oceans*, 125, e2019JC015764. <https://doi.org/10.1029/2019JC015764>, 2020.
- Perovich, D. K., and Polashenski., C.: Albedo evolution of seasonal Arctic sea ice, *Geophysical Research Letters*, 39, L08501, doi:10.1029/2012GL051432, 2012.
- 395 Pizzolato, L., Howell, S.E.L., Derksen, C., Dawson, J., and Copland, L.: Changing sea ice conditions and marine transportation activity in Canadian Arctic waters between 1990 and 2012, *Climatic Change*, 123, 161–173, doi:10.1007/s10584-013-1038-3, 2014.
- 400 Polashenski, C., Perovich, D.K., and Courville, Z.: The mechanisms of sea ice melt pond formation and evolution, *Journal of Geophysical Research*, 117, C01001, doi:10.1029/2011JC007231, 2012.
- Prinsenber, S.J and Hamilton, J.: Monitoring the volume, freshwater and heat fluxes passing through Lancaster sound in the Canadian Arctic Archipelago, *Atmosphere-Ocean*, 43:1, 1-22, DOI: 10.3137/ao.430101, 2005.
- 405 Rösel, A., Kaleschke, L., and Birnbaum, G.: Melt ponds on Arctic sea ice determined from MODIS satellite data using an artificial neural network, *The Cryosphere*, 6(2), 431–446. <https://doi.org/10.5194/tc-6-431-2012>, 2012.



- 410 Scharien, R. K., Hochheim, K., Landy, J., and Barber, D.G.: First-year sea ice melt pond fraction estimation from dual-polarisation C-band SAR – Part 2: Scaling in situ to Radarsat-2, *The Cryosphere*, 8, 2163–2176, <https://doi.org/10.5194/tc-8-2163-2014>, 2014.
- Scharien, R. K., Segal, R., Nasonova, S., Nandan, V., Howell, S.E.L. and Haas, C.: Winter Sentinel-1 backscatter as a predictor of spring Arctic sea ice melt pond fraction. *Geophysical Research Letters*, 44, <https://doi.org/10.1002/2017GL075547>, 2017.
- 415 Serreze, M.C., Holland, M.M. and Stroeve, J.: Perspectives on the Arctic's shrinking sea-ice cover, *Science*, 315: 1533–1536, 2007.
- Schröder, D., Feltham, D. L., Flocco, D., and Tsamados, M.: September Arctic sea-ice minimum predicted by spring melt-pond fraction, *Nature Climate Change*, 4(5), 353–357. <https://doi.org/10.1038/nclimate2203>, 2014.
- 420 Sigmund, M., Fyfe, J.C., Flato, G.M., Khariin, V.V. and Merryfield, W.J.: Seasonal forecast skill of Arctic sea ice area in a dynamical forecast system, *Geophysical Research Letters*, 40, 529–534, doi:10.1002/grl.50129, 2013.
- Small, D.: Flattening gamma: Radiometric terrain correction for SAR imagery, *IEEE Transactions on Geoscience and Remote Sensing*, 49(8), 3081–3093. <https://doi.org/10.1109/TGRS.2011.2120616>, 2011.
- Sou, T. and Flato, G.: Sea ice in the Canadian Arctic Archipelago: Modeling the past (1950–2004) and the future (2041–60), *Journal of Climate*, 22, 2181–2198, 2009.
- 430 Stroeve, J. C., Serreze, M.C., Holland, M.M., Kay, J.E., Maslanik, J., and Barrett, A.P.: The Arctic's rapidly shrinking sea ice cover: A research synthesis, *Climatic Change*, 110(3–4), 1005–1027, doi:10.1007/s10584-011-0101-1, 2012.
- Tivy, A., Howell, S.E.L., Alt, B., McCourt, S., Chagnon, R., Crocker, G., Carrieres, T., and Yackel, J.J.: Trends and variability in summer sea ice cover in the Canadian Arctic based on the Canadian Ice Service Digital Archive, 1960–2008 and 1968–2008, *Journal of Geophysical Research*, 116, C03007, doi:10.1029/2009JC005855, 2011.
- 435 Tschudi, M. A., Maslanik, J.A., and Perovich, D.K.: Derivation of melt pond coverage on arctic sea ice using MODIS observation, *Remote Sensing of Environment*, 112, 2605–2614, 2008.
- 440 Tschudi, M. A., Meier, W. N., and Stewart, J. S.: An enhancement to sea ice motion and age products at the National Snow and Ice Data Center (NSIDC), *The Cryosphere*, 14, 1519–1536, <https://doi.org/10.5194/tc-14-1519-2020>, 2020.
- Webster, M. A., Rigor, I.G., Perovich, D.K., Richter-Menge, J.A., Polashenski, C.M. and Light, B.: Seasonal evolution of melt ponds on Arctic sea ice, *Journal of Geophysical Research*, 120, 5968–5982, doi:10.1002/2015JC011030, 2015.
- 445

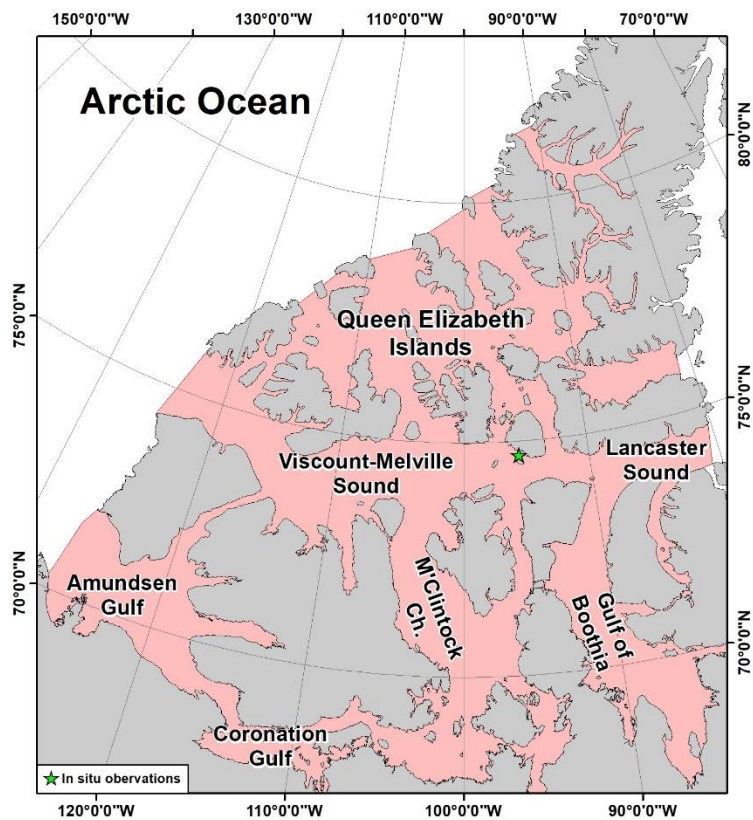


455 **Table 1.** Number of RADARSAT-2 images acquired over the Canadian Arctic Archipelago in April for 2009-2018.

Year	RADARSAT-2 Image Count
2009	90
2010	138
2011	149
2012	149
2013	188
2014	159
2015	133
2016	159
2017	151
2018	144

460

465



470 **Figure 1.** Map of the Canadian Arctic Archipelago region (red shading).

475

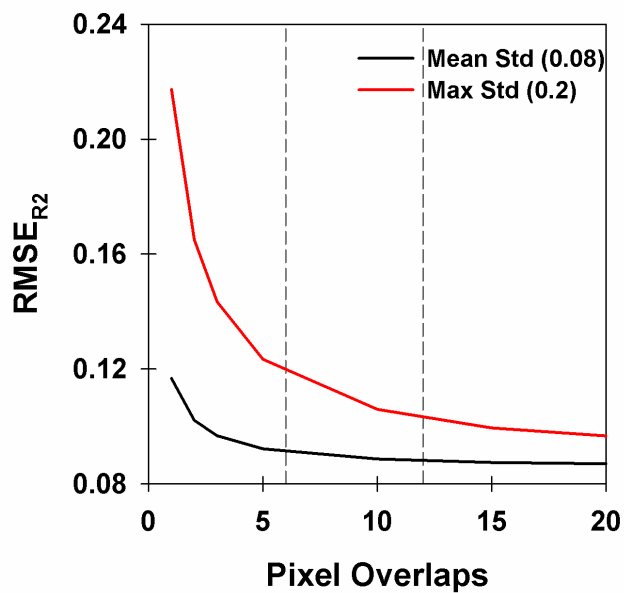


Figure 2. The root-mean square error of RADARSAT-2 melt pond fraction values ($RMSE_{R2}$) with increasing number of RADARSAT-2
480 pixel overlaps. The vertical dashed lines indicate the range of typical overlap from 2009-2018.

485

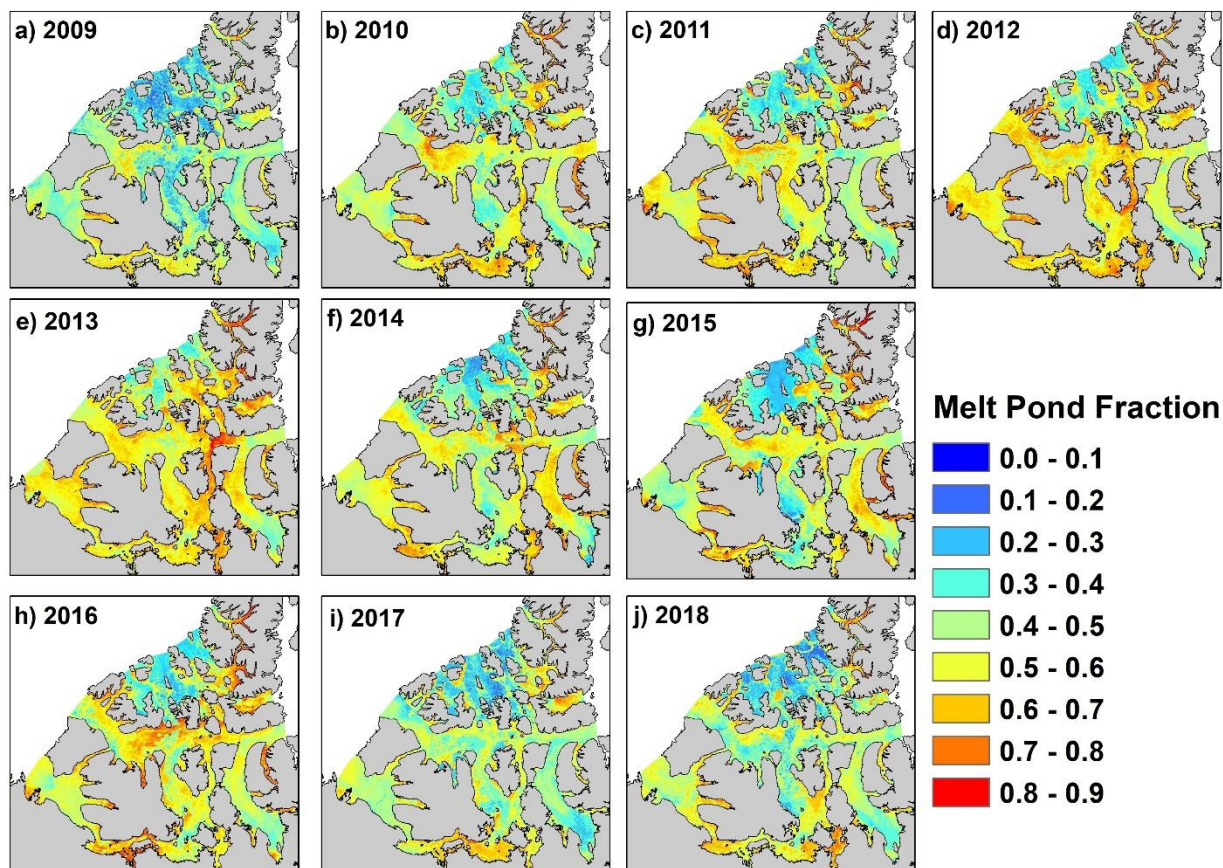


Figure 3. Spatial distribution of RADARSAT-2 melt pond fraction (f_p) in the Canadian Arctic Archipelago from 2009-2018 (a-j).

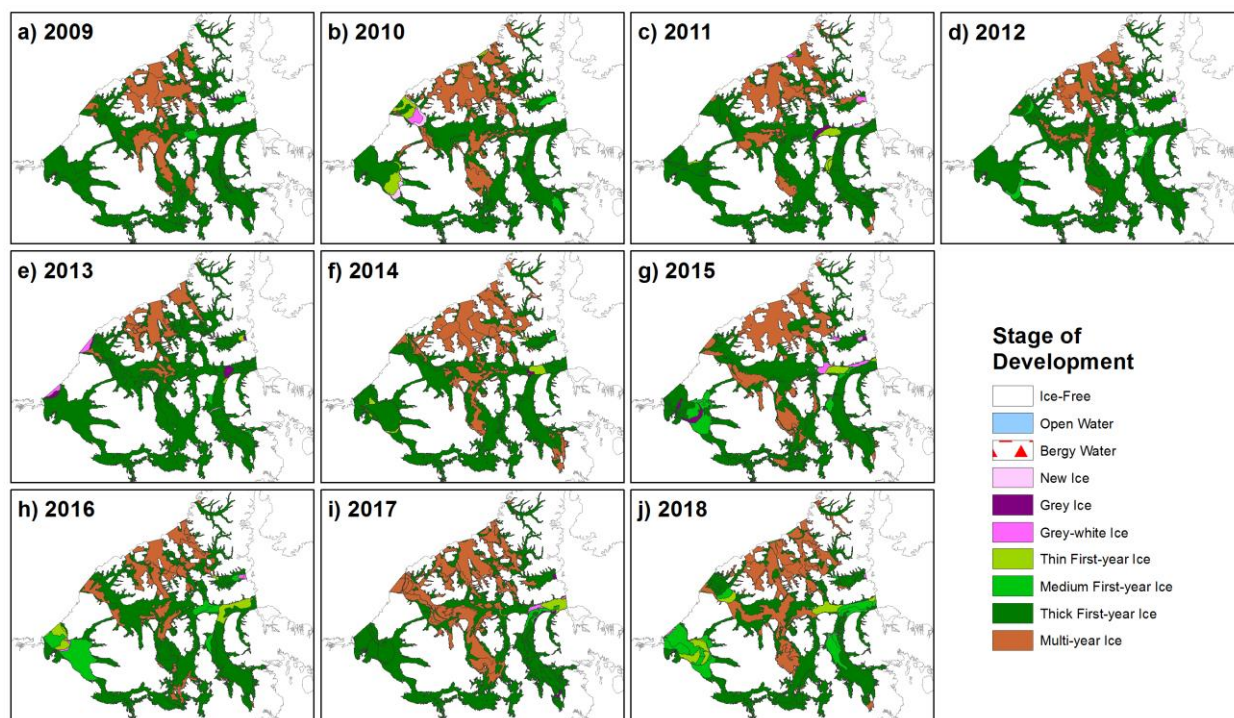
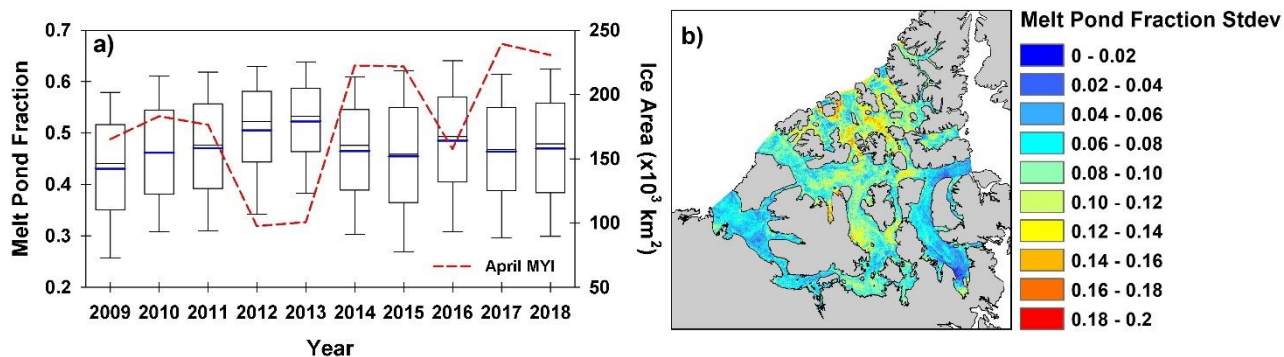


Figure 4. Spatial distribution of sea ice stage of development (type) on the first week of April in the Canadian Arctic Archipelago for 2009-2018 (a-j).

495

500

505

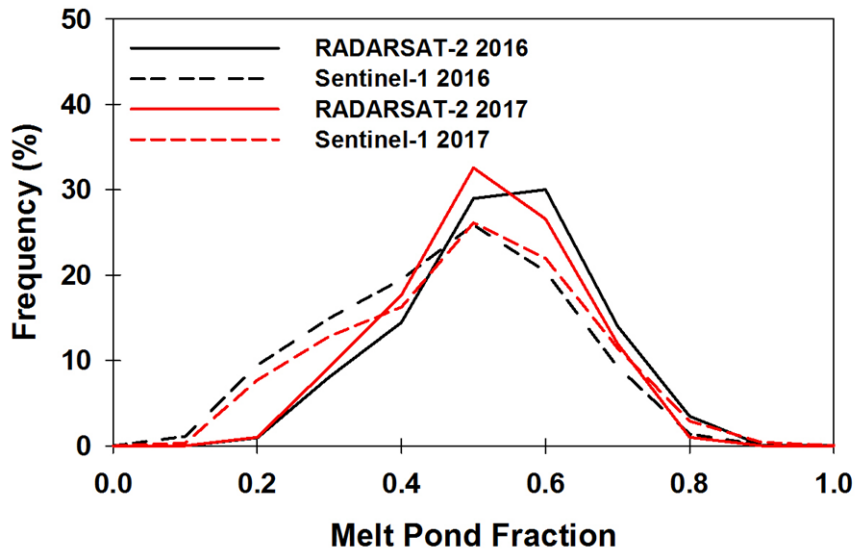


510 **Figure 5.** Boxplot time series of RADARSAT-2 melt pond fraction (f_p) and mean April multi-year ice (MYI) area in the Canadian Arctic
515 Archipelago for 2009-2018. The solid blue line represents the mean (a). Spatial distribution of the RADARSAT-2 f_p standard deviation
520 from 2009-2018 (b).

515

520

525



530

Figure 6. Frequency distribution (%) of RADARSAT-2 melt pond fraction (f_p) and Sentinel-1 f_p from Scharien et al. (2017) in the Canadian Arctic Archipelago for 2016 and 2017.

535

540

545

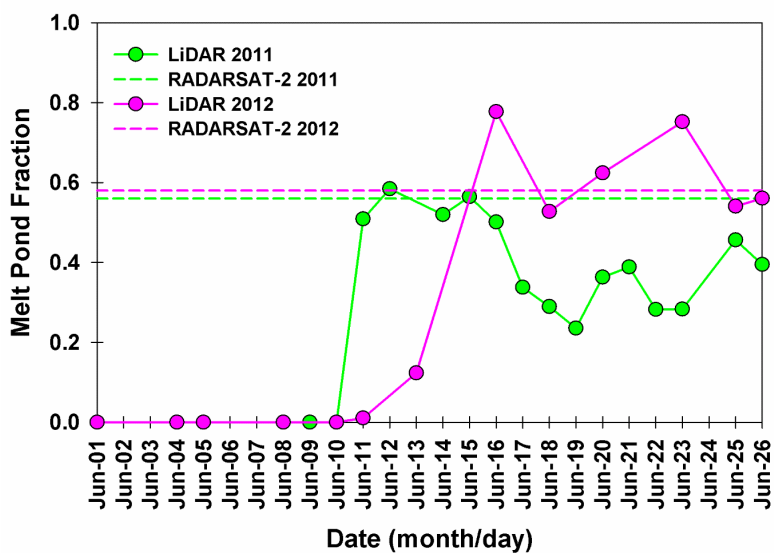
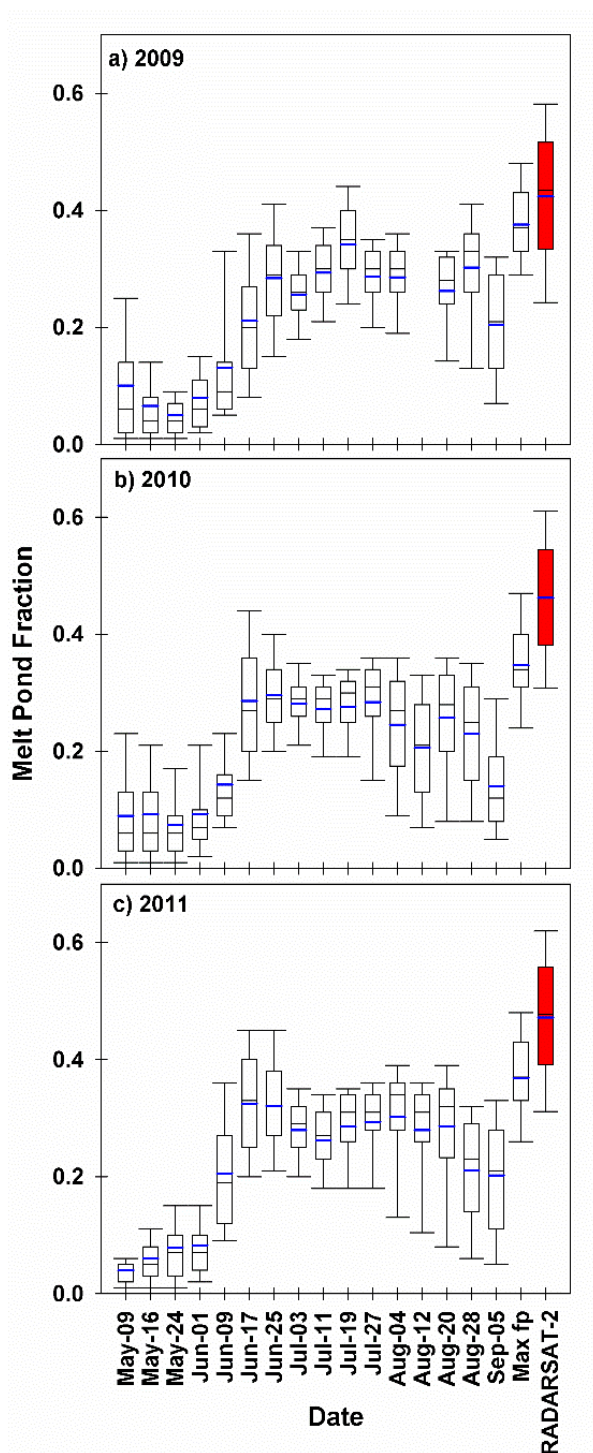
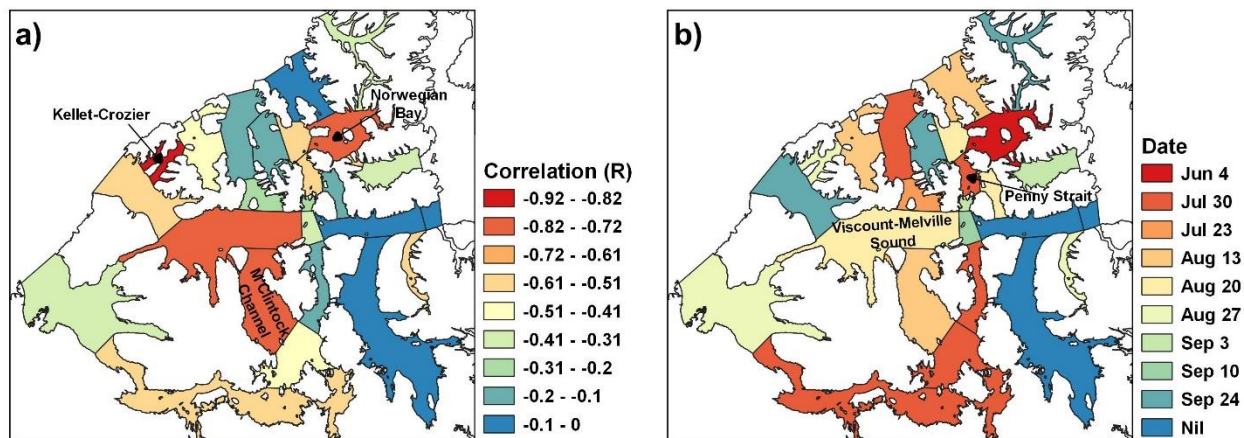


Figure 7. Temporal evolution of observed melt pond fraction (f_p) and RADARSAT-2 f_p at *in situ* observations sites for 2011 (74.7229°N; -95.1763°W) and 2012 (74.7264°N; -95.5772°W).



555

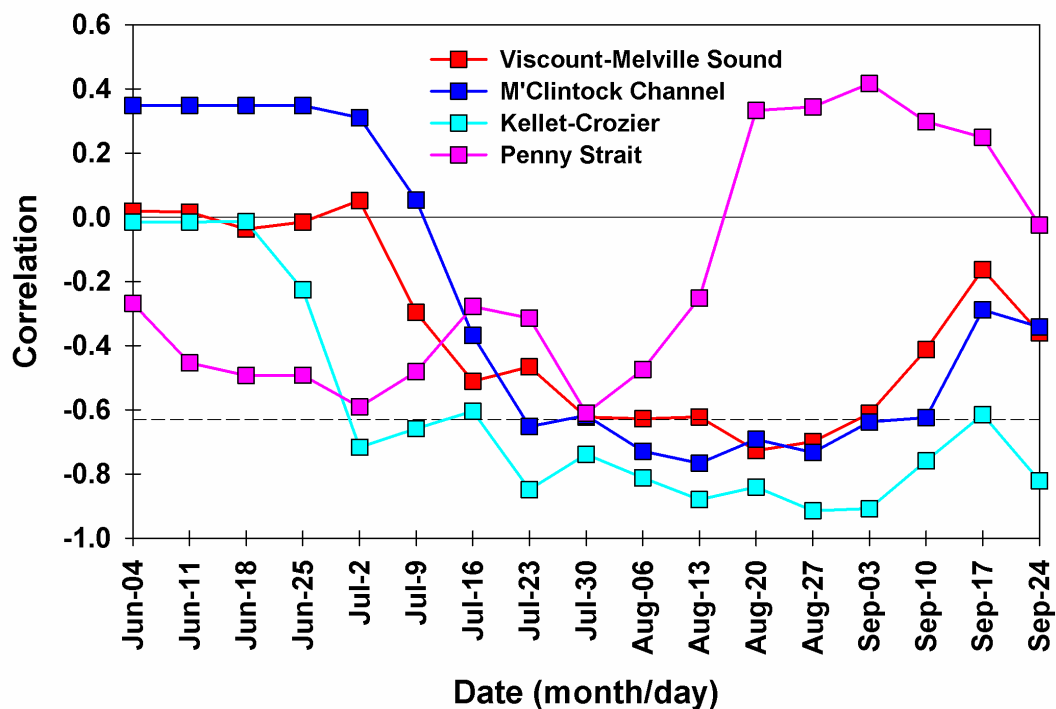
Figure 8. Boxplots of the seasonal time series of MODIS melt pond fraction (f_p), the maximum seasonal MODIS f_p and RADARSAT-2 f_p for (a) 2009, (b) 2010 and (c) 2011. The solid blue line represents the mean.



560 **Figure 9.** Spatial distribution of the (a) strongest detrended correlation (R) between RADARSAT-2 melt pond fraction (f_p) and weekly sea ice area and (b) week of occurrence.

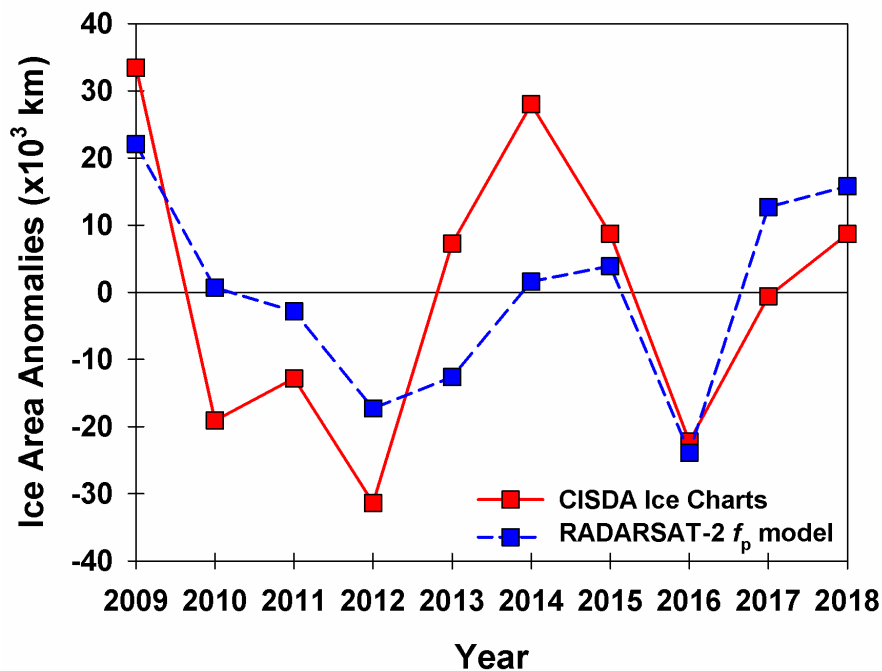
565

570



575 **Figure 10.** Time series of detrended correlations between RADARSAT-2 melt pond fraction (f_p) and weekly sea ice area for selected regions in the Canadian Arctic Archipelago from June to September. The dashed black line is statistical significance at the 95% confidence level.

580



585 **Figure 11.** Predicated sea ice area anomalies (detrended) using RADARSAT-2 melt pond fraction (f_p) and observed sea ice area anomalies (detrended) from the Canadian Ice Service Digital Archive (CISDA) ice charts in the Viscount-Melville Sound region of the Canadian Arctic Archipelago, 2009-2018.